frontiers | Frontiers in Water

TYPE Original Research
PUBLISHED 12 August 2022
DOI 10.3389/frwa.2022.925781

OPEN ACCESS

EDITED BY
Sarva Mangala Praveena,
Universiti Putra Malaysia, Malaysia

REVIEWED BY
Rahul Singh,
Lovely Professional University, India
Manraj Singh Cheema,
Universiti Putra Malaysia, Malaysia

*CORRESPONDENCE
Joseph A. Szule
jszule@cvm.tamu.edu

†These authors have contributed equally to this work

SPECIALTY SECTION
This article was submitted to Water and Human Health, a section of the journal Frontiers in Water

RECEIVED 21 April 2022
ACCEPTED 22 July 2022
PUBLISHED 12 August 2022

CITATION
Szule JA, Curtis LR, Sharpton TJ, Löhr CV, Brander SM, Harper SL, Pennington JM, Hutton SJ, Sieler MJ Jr and Kasschau KD (2022) Early enteric and hepatic responses to ingestion of polystyrene nanospheres from water in C57BL/6 mice. *Front. Water* 4:925781. doi: 10.3389/frwa.2022.925781

Early enteric and hepatic responses to ingestion of polystyrene nanospheres from water in C57BL/6 mice

Joseph A. Szule[1*†], Lawrence R. Curtis[2†], Thomas J. Sharpton[3,4], Christiane V. Löhr[5], Susanne M. Brander[6], Stacey L. Harper[2,7], Jamie M. Pennington[2], Sara J. Hutton[2], Michael J. Sieler Jr.[3] and Kristin D. Kasschau[3]

[1]Department of Veterinary Pathobiology, Texas A&M University, College Station, TX, United States, [2]Department of Environmental and Molecular Toxicology, Oregon State University, Corvallis, OR, United States, [3]Department of Microbiology, Oregon State University, Corvallis, OR, United States, [4]Department of Statistics, Oregon State University, Corvallis, OR, United States, [5]Department of Biomedical Sciences, Oregon State University, Corvallis, OR, United States, [6]Coastal Oregon Marine Experiment Station, Department of Fisheries, Wildlife, and Conservation Sciences, Oregon State University, Newport, OR, United States, [7]School of Chemical, Biological and Environmental Engineering, Oregon State University, Corvallis, OR, United States

Drinking water is one of numerous sources of human exposure to microscale and nanoscale plastic particles. Here, using a mouse model, we tested enteric and hepatic cellular responses to nanoplastic ingestion. At 1.5 or 25.5 h after an oral dose of 70 mg polystyrene nanospheres (PSNS)/kg (nominal diameters of 20 and 200 nm) in aqueous suspension female mice exhibit no overt signs of toxicity. Routine histopathology on small intestine and liver reveals no acute toxicity. Immunohistochemistry detects an increase in the number of enterocytes with cleaved caspase-3 (active form) after PSNS exposure ($p \leq 0.05$) indicating progression toward lytic cell death *via* a proinflammatory pathway. This is not evident in liver after PSNS exposure. Transmission electron microscopy detects lytic cell death in enterocytes at 25.5 h after 200 nm PSNS exposure. Putative endosomes in liver appear to sequester 20 and 200 nm particles 25.5 h after exposure. Both 20 and 200 nm PSNS appear in putative perinuclear autolysosomes 25.5 h after treatment. No significant changes in gene expression in the small intestine or liver 25.5 h were observed after dosing, but there was a trend toward altered expression of *cyp1b1* in the liver. Analysis of the fecal microbiome shows loss of diversity after exposure to both 20 and 200 nm particles after 25.5 h. Taken together, these results suggest risk from ingestion of nanoscale plastic particles from drinking water, which deserves systematic investigation.

KEYWORDS

nanoplastic, ingestion, enterocytes, hepatocytes, cellular trafficking, gene expression, gut microbiome, rodent model

Introduction

Micro- and nanoplastic water pollution

Plastic pollution, especially as micro- and nanoscale fragments, is a global concern, but risk to human health is unclear. Stubbins et al. project plastic-carbon equivalent growth accumulation in the Earth ecosystem from about 2 pg in 2000, to 14 pg in 2035, and 70 pg in 2095 (Stubbins et al., 2021). With current production estimates and waste plastic mitigation strategies, reduction in release rates for plastic pollution by 2030 appears unlikely (Borrelle et al., 2020). Because microplastic and nanoplastic disposal and formation in the environment are increasing, it follows that human exposure from drinking water, food, as well as indoor and outdoor air pollution are also increasing (Wright and Kelly, 2017; Revel et al., 2018; Brahney et al., 2021; Mohamed Nor et al., 2021). Only limited data in mammalian experimental animals on toxicity of nanoplastics are available (Deng et al., 2017; Yong et al., 2020), and while assessments of risk to humans from common exposure routes such as drinking water have been conducted, they are limited due to the current shortage of data (Coffin et al., 2022). A review of 305 field and laboratory studies on the potential for bioaccumulation of microplastics after ingestion indicates little biomagnification or trophic transfer (Gouin, 2020), but other findings suggest there is cause for concern and that further research is needed before ruling out the potential impacts of micro- and nanoplastics particularly given that they are now detected in human blood (Coffin et al., 2022; Leslie et al., 2022). There is negligible intestinal absorption of larger microplastics (>50 μm), but a paucity of analytical techniques for particles below this size (Brander et al., 2020; Cowger et al., 2020), and the fact that one cannot infer the intestine does not absorb smaller particles under 10 μm, necessitate additional data for these smaller particles.

The overarching objective of this work was to assess tissue- and cell type-specific fate, disposition, and toxicity of carboxylated polystyrene nanospheres (PSNS) of nominal 20 and 200 nm diameter in mice, ingested from dosed water. The basis for dosing (70 mg/kg) is an estimate of weekly ingestion of plastic by humans (Senathirajah and Palanisami, 2019; Senathirajah et al., 2021). Use of carboxylated PSNS provides a surrogate for environmental oxidation products, predominant steps in degradation pathways (Stubbins et al., 2021). A particular area of emphasis of this study was to characterize signs of cell-type specific interactions between PSNS with enterocytes of the proximal small intestine (duodenum and/or jejunum), liver sinusoidal endothelium, Kupfer cells, and hepatocytes, as well as to assess potential larger scale changes in the gut microbiome.

Methods

Polystyrene nanospheres

Carboxylated PSNS with nominal diameters of 20, 40, and 200 nm were purchased from Thermofisher Scientific (Waltham, MA). Nanosphere suspensions were dialyzed in 10 K MWCO SnakeSkin (Thermofisher Scientific) dialysis tubing against 5 L of gently stirred reverse osmosis product water, that was changed daily for 7 days. The final volume was diluted and yielded the final percentage of PSNS in 20 mM HEPES buffer, pH 7.4.

Animals treatments

Female C57BL/6 mice (20 g), purchased from Jackson Laboratories (Sacramento, CA), received a single gavage (0.2 ml) with PSNS 70 mg/kg in 20 mM Hepes buffer (pH 7.4) or buffer alone. Two mice received no gavage (naïve animals). After 1.5 or 25.5 h, mice were anesthetized with 5% isoflurane vapor until not responsive to paw pinch or a touch to the corner of the eye. An abdominal midline incision allowed cardiac puncture for blood draw (0.5 ml), and excision of the small intestine and medial lobe of the liver. Small fragments of jejunum and duodenum, and median lobe of the liver were fixed in: 10% neutral buffered formalin at room temperature; 2% glutaraldehyde (in pH 7.4 phosphate buffer) for 1 week at 4°C and transferred to 0.1 M sodium cacodylate (pH 7.2) for storage at 4°C; or RNA Later (Thermofisher Scientific) for 24 h at 4°C. RNA Later was decanted and tissue fragments were then stored at −80°C. There were 3 mice per treatment and 6 conditions.

Scanning electron microscopy

Plasma samples (5 μl) from mice that had undergone all treatments, and a 40 nm PSNS positive control, were transferred to carbon-coated 300 mesh copper grids and air-dried. They were examined by SEM (FEI Helios Nanolab instrument) in STEM mode using 30 kV and 25 na current. Magnification ranged from 25,000X to 35,000X. The readily observed 40 nm PSNS tended to aggregate but maintained spherical structure with distinct margins.

Histopathology and immunohistochemistry

Representative formalin-fixed tissue slices of liver and small intestine were processed overnight and embedded in paraffin. Separate composite blocks were generated containing pieces of liver, jejunum, or duodenum. Composite blocks of duodenum contained 1 tissue from 1 animal in each of the 6 groups

(vehicle, 20 and 200 nm from both 1.5 and 25.5 h timepoints) plus lung from a naïve animal for orientation, yielding three composite blocks. Six liver composite blocks were generated; each contained 1 naïve liver sample and 1 sample representing each treatment group at one of the timepoints (e.g., naïve; vehicle, 20 and 200 nm collected at 1.5 h).

Routine hematoxylin and eosin (H&E) stained sections (3–5 μm thick) of liver and small intestine (duodenum and jejunum) were examined by light microscopy. Digital images were taken (Nikon Eclipse 600 microscope and Nikon Digital Sight DS-Fi1; 2/3-inch, color, 5.24-megapixel) using the NIS-BR Elements imaging software (v21.1; www.nikonmetrology.com). One representative microphotograph was taken of each H&E stained sections at 200X magnification for side-by-side comparison of tissues across treatments.

Sections of liver, duodenum and jejunum (25.5 h groups only) were immunolabeled for cleaved caspase-3 using a Dako Autostainer Universal Staining System (Dako; Carpinteria, CA) according to standard operating procedures of the Oregon Veterinary Diagnostic Laboratory at OSU. Paraffin sections were high-temperature antigen retrieved with BDTM Retrieval A solution (Dako). Endogenous peroxidase activity was blocked by immersing slides in methanol containing 3% hydrogen peroxide for 10 min. Primary antihuman cleaved caspase-3 mouse monoclonal antibody (Dako M7051) was applied for 30 min at room temperature. MaxPoly-One Polymer HRP Mouse Detection solution (MaxVision Biosciences; Bothell, WA) was applied for 7 min at room temperature and Nova Red (SK-4800 from Vector Labs; Burlingame, CA) as chromagen was used with Dako hematoxylin (S3302) as counterstain. Serial sections of tissue incubated with Dako Universal negative serum served as negative controls for each sample. Serial sections of a mouse colon and spleen incubated with cleaved caspase-3 or incubated with Dako Universal negative serum were used as positive or negative method controls, respectively. All cells with a visible nucleus whose cytoplasm was diffusely immunolabeled red to dark red were counted and recorded for each liver section and for each transverse section of duodenum. Counts of immunolabeled enterocytes per section were analyzed by two-way ANOVA.

Transmission electron microscopy

PSNS staining and imaging

Nominal 20 and 200 nm PSNS suspended in water were prepared for transmission electron microscopy using two different protocols. (1) PSNS were stained with 0.1% ruthenium tetroxide (Electron Microscopy Sciences; Hatfield, PA) in 0.1M cacodylate buffer (pH 7.4) prior to being deposited on formvar/carbon coated copper grids (Electron Microscopy Sciences). (2) uranyl acetate was applied to the PSNS that had previously been deposited on formvar/carbon coated copper grids. Images were collected at magnifications ranging from 71,000X to 180,000X using an FEI Morgagni 268 transmission electron microscope operated at 70 keV and equipped with a MegaView III CCD camera.

Tissue preparation and imaging

Jejunum tissues were cut into ∼5 × 5 mm squares and liver tissues were diced into ∼5 × 5 × 5 mm cubes. The tissues were chemically fixed and stained with heavy metals by either of 2 methods. (1) a conventional method: 2% glutaraldehyde in 0.1 M cacodylate buffer (pH 7.4), 1% osmium tetroxide with 1% potassium ferrous cyanide in 0.1 M cacodylate buffer (pH 7.4) to accentuate the contrast of plasma membranes (Rivlin and Raymond, 1987), and saturated uranyl acetate *in situ*. (2) a modified method: 2% glutaraldehyde in 0.1 M cacodylate buffer (pH 7.4), and 1% osmium tetroxide with 0.1% ruthenium tetroxide in 0.1 M cacodylate buffer (pH 7.4) to preferentially stain PSNS (Trent et al., 1983). The tissues were dehydrated in increasing concentrations of ethanol and infiltrated with eponate-12 resin (Ted Pella Inc.; Redding, CA); the resin was initially dissolved in ethanol (Desai et al., 2010) to guard against dissolving the PSNS beads taken up by the tissues. Ultrathin tissue sections (∼100 nm in thickness; estimated by interference color) were cut using a Leica UC6 ultramicrotome and diamond knife (DiATOME; Hatfield, PA), and imaged using an FEI Morgagni 268 transmission electron microscope equipped with a MegaView III CCD camera. The contrast and brightness of the images were adjusted using Adobe Photoshop software to better visualize the structures of interest, however the data were not fundamentally altered. Measurements were made using ImageJ software (Schneider et al., 2012) (https://imagej.nih.gov/ij/).

Gene expression

RNA was isolated from liver and small intestine tissue using RNeasy columns (Qiagen; Hilden, Germany) and cDNA was synthesized using SuperscriptIII First-Strand Synthesis Supermix (11752-050). qPCR was performed on BioRad's CFX96 Real-Time System using SsoAdvancedUniversal SYBR Green Supermix (1725271). Expression of IL22, GR, Catalase, SOD1, Claudin2, Occludin, TJP1, and Cyp1b1 were normalized to GAPDH using approaches described in (Livak and Schmittgen, 2001; Garcia et al., 2018; DeCourten et al., 2019); see Supplementary Table 1 for primer sequences. RNA concentration (330.17 ± 32.98; mean ± standard error) and 260/280 ratios (>1.95) were quantified using a NanoDrop™ One/OneC Microvolume UV-Vis Spectrophotometer (ThermoFisher Scientific). $^{\Delta\Delta CT}$ values were used for data analysis and visualization. A one-way ANOVA followed by a Tukey *post-hoc* test was performed on samples.

Microbiome response

Microbial DNA was extracted from mouse fecal samples and 16S rRNA gene sequence libraries were produced and analyzed following established approaches (Kundu et al., 2021). Briefly, the DNeasy PowerSoil Pro DNA kits (Qiagen) were used to extract and purify DNA. The V4 region of the 16S rRNA gene was PCR amplified using the Earth Microbiome Project 16S index primers and protocols (Walters et al., 2016). PCR products were visualized on a 1.5% agarose gel and quantified on a Qubit 2.0 (Thermofisher Scientific) using the Qubit dsDNA HS Assay. One hundred ng of each PCR sample was pooled, cleaned using the QIAquick PCR Purification Kit (Qiagen), and quality was verified on the Agilent TapeStation 4200. The prepared library was submitted to the Oregon State University Center for Quantitative Life Sciences (CQLS) for 300 bp paired-end sequencing on an Illumina MiSeq System (RRID:SCR_016379). All microbiome DNA sequence analyses and visualizations were conducted in R (v 4.0.1). Fastq files were processed in using the DADA2 R package (v 1.18.0). Briefly, forward and reverse reads were trimmed at 280 and 230 bp, respectively, subsequently merged into contigs, and subject to amplicon sequence variant (ASV) identification. ASVs unannotated at the Phylum level were removed to result in 292 remaining detected ASVs. Alpha-diversity was calculated using the estimate_richness function (Phyloseq v 1.38.0) and transformed using Tukey's Ladder of Powers. After transformation, scores were normalized from 0 to 1 by dividing each score by the maximum value, which allowed us to compare results across alpha-diversity metrics using general linear models (GLMs). Two-way ANOVA assess these GLMs. Beta-diversity models were generated using methods described previously (Kundu et al., 2021). Briefly, we evaluated three beta-diversity metrics—Bray-Curtis, Canberra, and Sorenson—and resolved the relationship between experimental parameters and beta-diversity by applying a step-wise model selection approach as implemented in the capscale function (vegan package v2.5). Optimal models were subsequently subject to PERMANOVA analysis to determine if the selected model parameters significantly explained the variation in microbiome composition across samples.

Results

PSNS exposure affects enterocytes of the small intestine

For histopathology on small intestine after ingestion of 20 and 200 nm PSNS, no differences were identified in side-by-side comparisons between treatment groups using photomicrographs of H&E stained sections, and all samples of small intestine appeared within normal limits. Total counts of duodenal enterocytes immunolabeled for cleaved caspase-3 were not statistically different among groups. However, when counts of cleaved caspase-3 immunolabeled cells in the duodenum were pooled with those in the jejunum (25.5 h groups only) from these same mice, a statistically significant difference ($p = 0.0492$) existed between PSNS treated and vehicle controls (Figures 1A,B, Table 1; Supplementary Table 2). Pooling was justified since the two sections of small intestine were immediately adjacent and trends for counts within treatment groups were similar within them. There was no effect of time on scores within groups treated with the same PSNS size. By qualitative TEM assessment on tissue stained by the conventional method, there appeared to be an increased proportion of enterocytes that were damaged or undergoing cell death 25.5 h after ingestion of 200 nm PSNS (Figure 1C) when compared to control, but not after ingestion of 20 nm PSNS.

The effective diameters of isolated control 20 and 200 nm PSNS, after staining with ruthenium tetroxide and imaged by TEM, were 20.9 ± 6.7 nm ($n = 228$) and 247.4 ± 57.7 nm ($n = 242$), respectively (Supplementary Figure 1). Jejunum, stained with the modified method using ruthenium tetroxide as an effective chromagen to visualize PSNS (Trent et al., 1983) with osmium tetroxide as an effective counterstain, was also imaged by TEM (Figure 2). At the interface between the intestinal lumen, the microvilli, and the intracellular regions of enterocytes, round structures that were densely stained above background, referred to here as densities, were measured and tabulated if between 14.2 and 27.6 nm and between 189.7 and 305.1 nm (i.e., within 1 standard deviation of the control PSNS diameters); see Table 2. There were appreciable increases in the concentrations of densities that have diameters within 1 standard deviation of the 20.9 ± 6.7 nm beads (referred to as small densities) in the lumen (2.4-fold increase), microvilli (3.3-fold increase), and intracellular regions (2.5-fold increase) between control mice and mice that ingested 20 nm PSNS. There were no increases in the concentrations of small densities in the lumen, microvilli or intracellular regions between control mice and mice that ingested 200 nm PSNS. There were modest increases that are not likely to be relevant in the concentration of densities that have diameters within 1 standard deviation of the 247.4 ± 57.7 nm PSNS (referred to as large densities) in intracellular regions between control mice and mice that ingested 20 nm PSNS (1.5-fold increase), and between control mice and mice that ingested 200 nm PSNS (1.7-fold increase). There were no increases in the concentrations of large densities in the lumen or microvilli between control mice and mice that ingested 200 nm PSNS.

PSNS uptake by hepatocytes

To test whether the ingested PSNS had crossed the gut barrier and gained access to the bloodstream, scanning electron

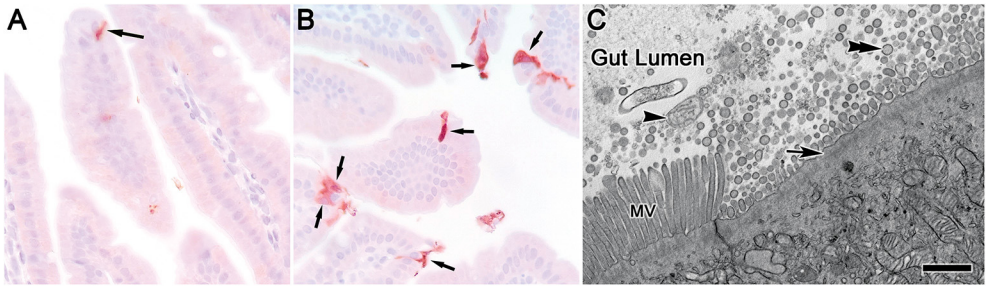

FIGURE 1
Mouse small intestine enterocytes after exposure to 200 nm PSNS. Enterocytes immunolabeled for cleaved caspase-3 [arrows in **(A,B)**] 1.5 h after gavage with **(A)** vehicle control and **(B)** 200 nm PSNS. Nova red as chromagen and hematoxylin as counter stain. **(C)** Enterocytes from mouse small intestine (jejunum) 25.5 h after gavage with 200 nm PSNS, fixed and stained by the conventional method, and imaged by transmission electron microscopy. An enterocyte is showing signs of lytic cell death (arrow) with blebs of putative apoptotic bodies (double arrowhead) and mitochondria (arrowhead) in the gut lumen. Note the microvilli (MV) of an adjacent enterocyte. Scale = 30 μm in **(A,B)**; 1 μm in **(C)**.

TABLE 1 **Immunohistochemistry for cleaved caspase-3 (activated) in small intestine of mice after gavage of aqueous vehicle alone (Control), nominal 20 nm, or 200 nm PSNS.**

	Treatment*		
Time after treatment (hours)	**Control**	**20 nm PSNS**	**200 nm PSNS**
1.5	2.3 ± 1.1	5.5 ± 1.9	6.3 ± 3.0
25.5	1.3 ± 0.6	6.0 ± 2.4	5.0 ± 1.6

Mean ± Standard Error for counts of cleaved caspase-3 immunolabelled enterocytes in transverse sections of small intestine from female C57BL6 mice. Mice (n = 3) were euthanized 1.5 or 25.5 h after treatments and segments of small intestine were processed for examination by light microscopy (Methods). Duodenum sections from all mice were scored. In addition, jejunum sections from each mouse euthanized 25.5 h after treatment were scored. Two-way analysis of variance detected no effect of time on scores within treatment groups (vehicle, 20 nm, 200 nm). However, there was a statistically significant (*) treatment effect (p = 0.0492) when samples from both timepoints were combined.

microscopy was conducted on plasma drawn from mice that had ingested vehicle buffer, 20 nm PSNS and 200 nm PSNS by gavage. No structures similar to 20 or 200 nm PSNS were observed from mice euthanized 1.5 or 25.5 h after gavage (not shown). These results suggest that the PSNS had either not gained access to the blood, was below detection threshold in plasma, or was rapidly cleared. Presence of both sizes of PSNS in liver 25.5 h after gavage demonstrates their systemic distribution (see Discussion). In H&E stained sections, all livers had minimal to mild cytoplasmic, poorly defined vacuoles in hepatocytes (minimal vacuolar change without zonal pattern) and rare foci of extramedullary hematopoiesis. A single hepatocyte was immunolabeled in one of the livers collected 25.5 h after treatment with 200 nm PSNS (not shown).

By TEM on conventionally stained livers, there were indications that both 20 and 200 nm PSNS had been processed by hepatocytes (Figure 3). Clusters of tubule-like structures, consistent in appearance with endosomes, were apparent and their diameters were unchanged between control mice (84 ± 19 nm), mice that ingested 20 nm PSNS (75 ± 8 nm), and mice that ingested 200 nm PSNS (78 ± 8 nm). At higher magnification, the tubule-like structures from mice that ingested 20 nm PSNS, but not control mice or mice dosed with 200 nm PSNS, contained circular structures 26 ± 4 nm ($n = 50$) in diameter (Figure 3A) that were not significantly different from similarly stained control 20 nm PSNS (28 ± 6 nm, $n = 20$; $p = 0.11$). Further, in hepatocytes from mice that had ingested 200 nm PSNS, there were regions with large vacuoles that contained circular structures that are similar in size to the 200 nm PSNS (Figure 3B).

Large perinuclear structures in hepatocytes contained round densities that were readily identified by TEM on livers stained with ruthenium tetroxide as an effective chromagen to visualize PSNS (Trent et al., 1983; Figure 4). The diameters of the perinuclear structures were not different in hepatocytes from vehicle gavaged control mice (680.9 ± 190.7 nm; $n = 13$), mice that ingested 20 nm PSNS (687.5 ± 168.7 nm; $n = 17$) and mice that ingested 200 nm PSNS (719.8 ± 221.9 nm; $n = 21$). However, from control mice, densities in perinuclear structures had diameters of 102 ± 36.8 nm ($n = 63$), which were significantly different from the diameters of either the 20 nm PSNS ($p < 0.0001$; t-test) and 200 nm PSNS ($p < 0.0001$; t-test) similarly stained with ruthenium tetroxide. From mice that ingested 20 nm PSNS, small densities in perinuclear structures had diameters of 25.5 ± 8.7 nm ($n = 109$), which were not significantly different than the similarly stained 20 nm PSNS ($p < 0.0001$; t-test). And, from mice that ingested 200 nm PSNS, large densities in perinuclear structures had diameters of 224.0 ± 41.5 nm (mean ± S.D; $n = 42$), which were not significantly different than the similarly stained 200 nm PSNS ($p < p < 0.01$; t-test). These data indicate that the PSNS beads ingested by the mice are accumulating in hepatocyte perinuclear organelles that are morphologically similar to lysosomes.

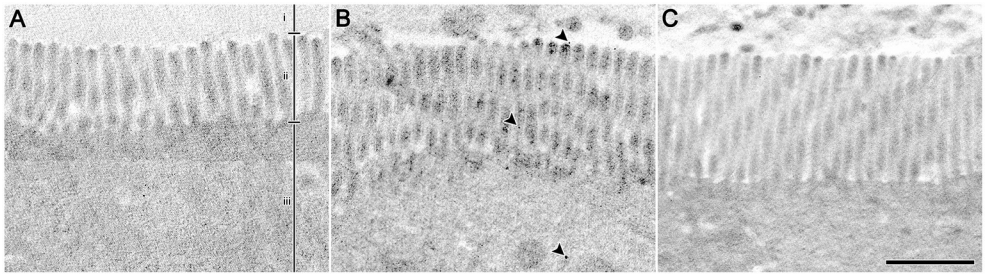

FIGURE 2
Enterocytes from mouse jejunum stained with ruthenium tetroxide, counterstained with osmium tetroxide, and imaged by transmission electron microscopy. Example images showing the interface between the intestinal lumen (i), the microvilli (ii), and the intracellular regions of enterocytes (iii). **(A)** From a control mouse that ingested aqueous vehicle. **(B)** From a mouse that ingested 20 nm PSNS; arrowheads indicate examples of densities with diameters ranging between 14.2 and 27.6 nm. **(C)** From a mouse that ingested 200 nm PSNS. Scale = 1 μm.

TABLE 2 Accumulation of densities, visualized by electron microscopy, in the jejunum of mice after ingestion by gavage of aqueous vehicle alone (Control), and nominal 20 nm and 200 nm PSNS.

	Total area (μm^2)	20 nm densities/μm^2	200 nm densities/μm^2
Control			
Intestinal Lumen	95.8	0.084	0
Microvilli	153.4	0.117	0
Intracellular	316.2	0.130	0.003
Nominal 20 nm PSNS			
Intestinal Lumen	100.7	0.199	0.009
Microvilli	104.6	0.392	0
Intracellular	427.0	0.319	0.005
Nominal 200 nm PSNS			
Intestinal Lumen	231.7	0.073	0.009
Microvilli	252.3	0.087	0.004
Intracellular	1081.3	0.056	0.006

Densities that have diameters within 1 Standard Deviation of the nominal 20 nm PSNS (between 14.2 and 27.6 nm) and the nominal 200 nm PSNS (between 189.7 and 305.1 nm) in the "Intestinal Lumen," associated with the "Microvilli" and "Intracellular" to the enterocytes (see Figure 2). Although there is no biological replication of this experiment, images were collected from random positions in the jejunum for each exposure group (9 positions from control, 6 positions from 20 nm PSNS exposure, and 10 positions from 200 nm PSNS exposure) and expressed as cumulative values. Qualitatively, there appears to be more 20 nm densities in all 3 regions of jejunum after ingesting 20 nm PSNS, and a negligible increase of 200 nm densities after ingesting 200 nm beads, as compared to the other exposure groups.

Effects of PSNS exposure on enterocyte and hepatocyte gene expression

Gene expression analysis revealed no significant differences between the controls and treatment groups in the liver or small intestine (Supplementary Figure 2; $p > 0.05$, $n = 3$, one-way ANOVA, Tukey *post-hoc*) for 4–6 genes. In the liver, expression of *cyp1b1* was marginally different between the treatment groups exposed to 20 and 200 nm PSNS ($p = 0.078$). When compared to controls, expression of *cyp1b1* was slightly higher after exposure to 200 nm PSNS and slightly lower after exposure to 20 nm PSNS. Effect size is an alternate parameter to measure differences between treatment groups, and it was calculated using *Cohen's d* formula (McShane et al., 2019). The effect size for the difference between *cyp1b1* expression after exposure to 20 and 200 nm PSNS was 1.524351, which is considered large (i.e., >0.8). This discrepancy is likely due to the small sample size available for RNA extraction ($n = 3$) and the brevity of PSNS exposure.

PSNS exposure rapidly impacts microbiome diversity and composition

We collected fecal samples and used 16S rRNA gene sequencing to investigate how the mouse gut microbiome diversity and composition may be influenced by PSNS exposure as well as whether the size of the PSNS (20 or 200 nm) elicits specific effects. To assess microbiome biodiversity, we used generalized linear mixed effects models (GLMs) to identify parameters, such as plastic diameter, that best explained the variation in either the Simpson's and Shannon Indices of diversity (Figure 5A). Our analysis found that exposure to PSNS associates with reduced biodiversity of the gut microbiome as measured by both indices (Simpson's: $F = 7.34$, $p = 0.007$; Shannon: $F = 4.61$, $p = 0.032$). Moreover, we found that the size of the PSNS particles elicited specific effects on biodiversity, as the Simpson's index significantly differed between 20 and 200 nm particles ($F = 7.10$, $p = 0.029$). The Shannon diversity index did not quite reach our threshold for statistical significance ($F = 4.87$, 0.088).

We also observed that exposure to PSNS effects the composition of the gut microbiome and that these effects are particle-size dependent (Figure 5B). We used the Bray-Curtis dissimilarity metric, which measures the differences in community composition between a pair of communities in

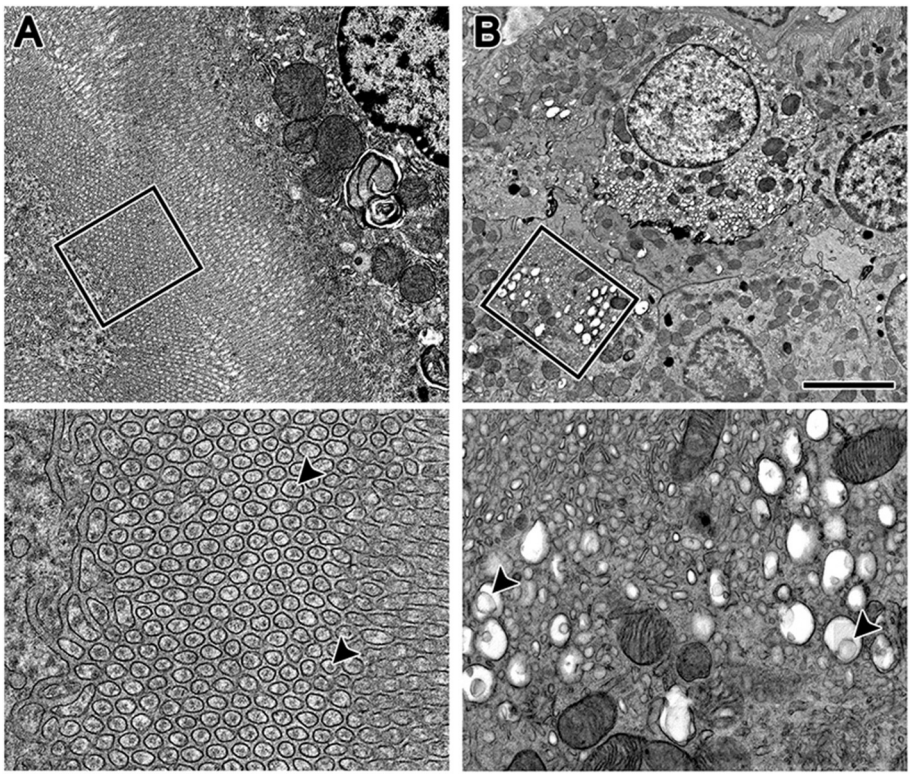

FIGURE 3
Mouse hepatocytes after ingestion of 20 and 200 nm PSNS, fixed and stained by the conventional method, and imaged by transmission electron microscopy. **(A)** Top panel: Lawns of tubule-like structures in hepatocytes were apparent in livers after ingesting 20 nm PSNS, as well as after ingesting control vehicle and 200 nm PSNS. However, after ingesting 20 nm PSNS only, increased magnification by 4X (boxed region; bottom panel) revealed that each tubule contained round particles (arrowheads) that were similar in diameter to the 20 PSNS that were ingested. **(B)** Top panel: After ingesting 200 nm PSNS, there were large vacuoles present in many of the hepatocytes. Increased magnification by 4X (boxed region; bottom panel) revealed that several of the vacuoles contained large circular structures that were similar in diameter to the 200 nm PSNS that were ingested. For example, the circular structure indicated by the arrowhead on the left side of the panel is 226 nm in diameter, and on the right side of the panel is 213 nm in diameter. Scale: **(A)** top = 2 μm, bottom = 500 nm; **(B)** top = 4 μm, bottom = 1 μm.

an abundance weighted fashion, to conduct our assessment of community composition. A PERMANOVA test revealed that gut microbial communities exposed to PSNS are significantly different in their composition relative to unexposed controls ($p = 0.017$). Additionally, we found evidence of particle-size specific effects on microbiome composition ($p = 0.035$). We followed up this analysis with similar tests using the Canberra and Sorensen measures of beta-diversity, which are more likely to resolve differences in composition that result from the less abundant taxa. These analyses found less evidence for differences in microbiome composition as a function of exposure or particle size with the exception being a link between exposure and the Canberra distance ($p = 0.017$). However, lack of significance in the above tests could be due to the small sample sizes included in this study. Indeed, our PERMANOVA tests of the relationship between PSNS particle diameter and the Canberra or Sorenson metrics result in small, but insignificant, p-values, which indicates that expanding the number of samples in future experiments may reveal that different PSNS exposure conditions differentially affect microbiome composition for these measures of beta-diversity. Overall, our results suggest that PSNS may rapidly impact the diversity and composition of at least the abundant members of the gut microbiome.

Discussion

It is difficult to overstate the complexity of assessing the ecological and human health risks of nanoplastic pollution. The five most abundant plastics on Earth (polyethylene, polypropylene, polyethylene terephthalate, polyvinyl, and polystyrene) differ in material properties including: density, photoreactivity, and bioreactivity (Stubbins et al., 2021). Environmental degradation of these polymers yields particles of different sizes, shapes, and surface chemistry, such as oxidized groups. Environmental exposures to such degradation products are complex mixtures, of which we argue nanoplastics are toxicologically significant. However, quantification of

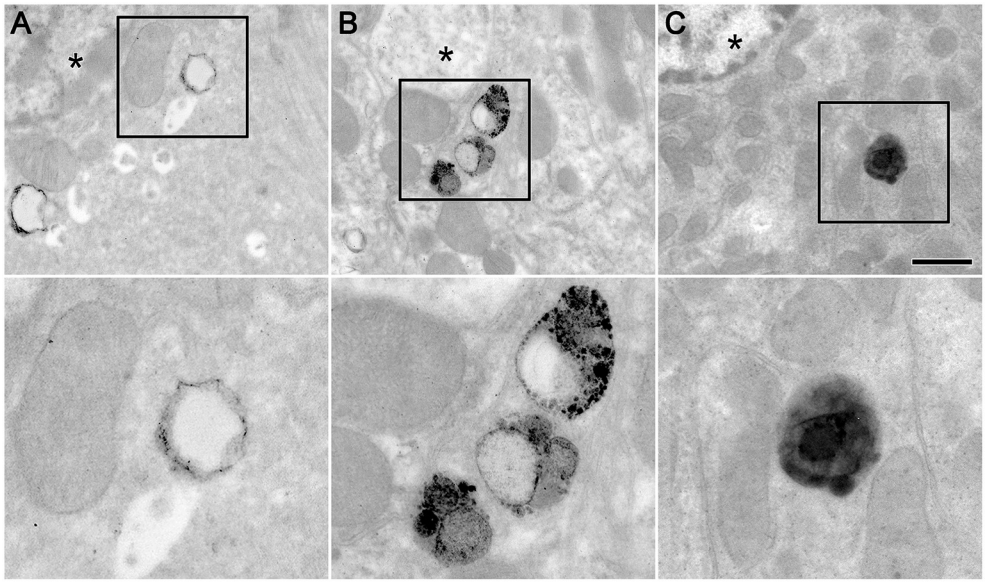

FIGURE 4
Hepatocytes from mouse livers that were stained with ruthenium tetroxide, counterstained with osmium tetroxide, and imaged by transmission electron microscopy. Example images from **(A)** a control mouse that ingested aqueous vehicle, **(B)** a mouse that ingested 20 nm PSNS, and **(C)** a mouse that ingested 200 nm PSNS. Structures that resemble lysosomes, highlighted in the boxed areas, were observed in close proximity to the nucleus (*). The boxed areas were magnified by 2.5X and displayed in the lower panels. Scale = 1 μm (top panels) and 400 nm (bottom panels).

nanoplastic particles is currently not feasible (see below). We study commercially available PSNS herein as a prototypical oxidized polymer at the nanoscale.

Senathriajah and Palanisami estimate a human microplastic ingestion global average of about 5 g a week (Senathirajah and Palanisami, 2019). Assuming a 70 kg person, this is about 70 mg/kg/week. Other work estimates inhalation and diet contribute a substantial fraction of total microplastic exposures in humans and that drinking bottled water dominates exposure in that medium (Cox et al., 2019). No such estimates for human consumption of nanoplastics are available. This lack of insight largely results from limitations on analyses of environmental and animal nanoplastic contamination including quantification. Diversity of plastics particles by size and polymer chemistry, and thresholds of resolution for nanoparticles at about 10 μm by spectral methods (Adar et al., 2005; Lasch and Naumann, 2006) are important parameters to consider. The use of the 70 mg/kg dose for this acute study is therefore a default assumption that it is environmentally relevant over the long-term. High doses are common for acute studies to set dose ranges for longer term toxicology studies. Work to determine the persistence (half-life) of nanoplastic particles in tissues including liver are needed to explain their tissue- and cell type-specific bioaccumulation potential.

There is size-dependent tissue distribution of microplastics and nanoplastics in mice and many species of fish (Wright and Kelly, 2017). Al-Sid-Cheikh provides an example using radiolabeled PSNS and quantitative whole-body autoradiography in a marine invertebrate, the scallop (Al-Sid-Cheikh et al., 2018). After waterborne exposure to a mixture of PSNS and algae (stimulates filter feeding), 250 nm PSNS is largely distributed to feeding and digestive structures, while 24 nm PSNS is distributed to all tissues. No PSNS of either size were visible by SEM in plasma from mice 1.5 or 25.5 h after gavage (Results). The possible explanations include (1) PSNS are not appreciably absorbed from the gut, (2) PSNS primarily associate with the cellular fraction of blood (pellet after centrifugation) rather than the supernatant (plasma), and (3) Rapid clearance of PSNS from blood. The presence of ruthenium tetroxide stained spherical structures in hepatocytes of mice treated with both 20 and 200 nm PSNS at 25.5 h after gavage indicated their systemic distribution, and favors the latter explanation. Transfer of PSNS across the gut wall into blood offered the only plausible explanation. TEM detected 20 nm structures within enterocytes of jejunum, but not 200 nm structures, suggesting their transfer across the gastrointestinal tract. Increased cell death of enterocytes after exposure to 200 nm PSNS suggests a compromised physical barrier. Binding to receptors in clathrin-coated pits and subsequent endocytosis are the initial steps in endosomal processing of cargo from blood (Schulze et al., 2019). The 50 nm diameter of clathrin-coated pits on the hepatocyte plasma membrane may explain appearance of 20 nm but not 200 nm PSNS in putative endosomes. A recent report in cell culture (Sommi et al., 2021) demonstrates a role

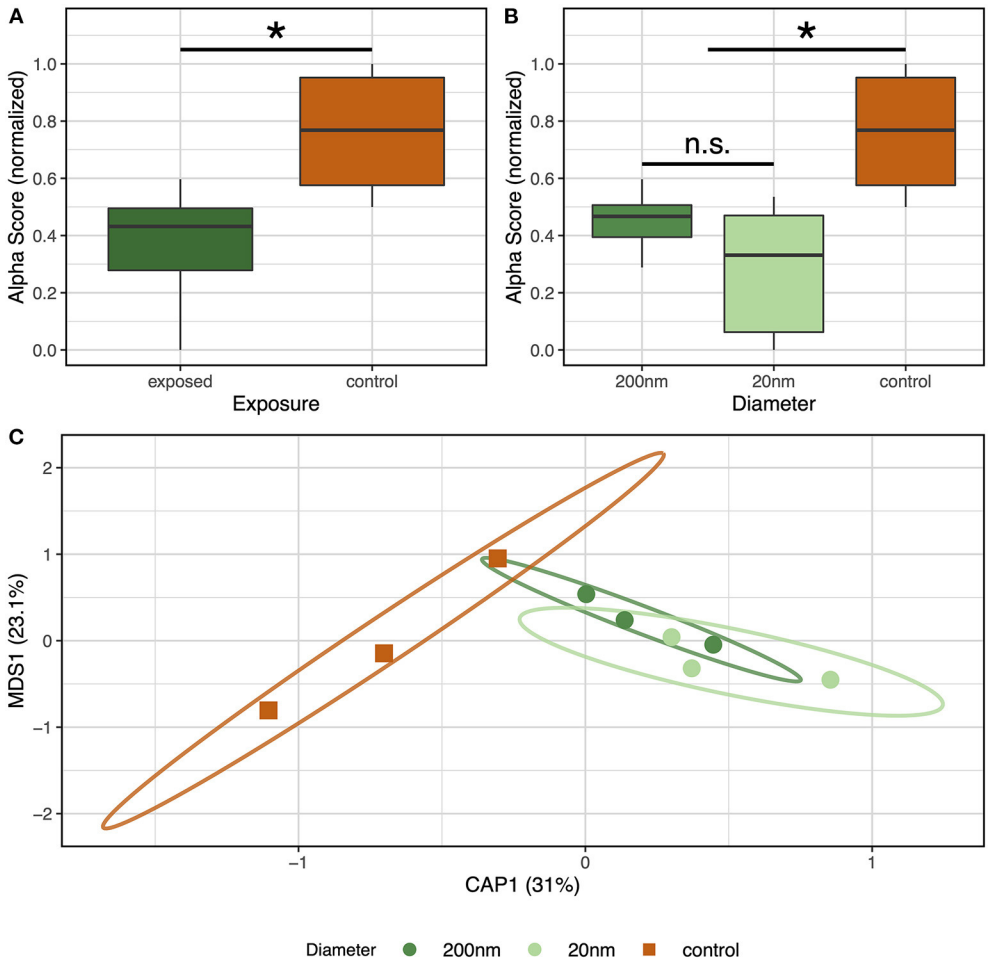

FIGURE 5
Effects of 20 and 200 nm PSNS on gut microbiome biodiversity and composition. Simpson's and Shannon Indices of diversity shows that gut microbiome biodiversity is significantly reduced in mice that were **(A)** exposed to PSNS and **(B)** the size of the particle effects the severity of reduction. *Indicates significant difference ($p < 0.05$). **(C)** Capscale ordination based on the Bray-Curtis dissimilarity of gut microbiome composition. The analysis shows that gut microbiome composition significantly differs as a function of PSNS exposure and particle size.

for microvillus-mediated adhesion as an alternative route for internalization of nanoparticles with an upper diameter limit of 70–80 nm. Further, a polyanionic surface is necessary for this interaction. Internalization itself involves endocytosis of segments of microvilli or buds thereof. A potential entry route for 200 nm PSNS into hepatocytes is initial endocytosis by a scavenger receptor of the sinusoidal endothelial cells (Pandey et al., 2020), transcytosis, and exocytosis for delivery to hepatocyte receptor/vesicle-based sorting machinery (Schulze et al., 2019). Interestingly, size-specific PSNS exposure induced a trend toward differences in liver *cyp1b1* gene expression, which encodes a phase I detoxification enzyme (reviewed in Hodges and Minich, 2015). Although this effect was not significant, yet had an effect size of 1.524351 based on Cohen's *d*, it aligns with findings from other studies assessing the impact of styrene oxide or microplastic exposure on vertebrates where *cyp1b1* or *cyp1a* were differentially expressed in the liver (Granby et al., 2018; Chatuphonprasert and Jarukamjorn, 2021). Accordingly, we hypothesize that ingestion of PSNS activates phase I metabolism pathways.

The long-term implications of hepatic disposition of 20 nm PSNS or other nanoplastic particles in putative endosomes deserve further investigation. Environmentally persistent nanoplastic particles are most likely recalcitrant to hepatocellular degradation. Endocytic trafficking of cargo can follow several different pathways (Naslavsky and Caplan, 2018), with 4 compelling scenarios in support of this notion. (1) Early endosomes undergo membrane fusion events during maturation to lysosomes where diverse proteolytic enzymes degrade cargo in this acidic compartment. PSNS degradation in this compartment is doubtful. Both 20 and 200 nm PSNS occur in perinuclear vesicles we consider putative

autolysosomes in hepatocytes. After nanoparticle treatment of primary hepatocytes, Zhang et al. identified autolysosomes by colocalization of immunostaining for LAMP1and a fluorescent dye (LysoTracker) (Zhang et al., 2017). These lysosomal structures persisted throughout the 12–48 h time-course of the experiment. The same group also show an association of large, persistent autolysosomes in liver with nanoparticle treatments of mice. Whether recalcitrant cargo in acidified lysosomes results in cell injury is an open, but important, question. (2) Recycling occurs between early endosomes and the Golgi. In addition, cargo modified in the Golgi can undergo direct secretion into extracellular fluid. (3) There is a fast pathway from early endosomes to extracellular fluid. (4) There is a slow pathway whereby cargo in early endosomes translocate to an endocytic recycling compartment before transport to extracellular fluid. Movement of nanoplastic in pathways 2, 3, or 4 might create a futile cycle between the hepatocyte and extracellular fluid or redistribution to other cell types.

Discerning the impact of nanoplastic particle consumption on the composition of the gut microbiome is relevant given the apparent ubiquity and frequency of exposure. In particular, gut microbes contribute to the physiology of higher organisms (Round and Mazmanian, 2009), and environmental factors can perturb the gut microbiome to result in chronic diseases, especially immune-related disorders (Kostic et al., 2014; Lu et al., 2014; Tu et al., 2020). While prior work has revealed the impact of microplastic consumption on the gut microbiomes of zebrafish (Wan et al., 2019), mice (Li et al., 2020), and humans *in vitro* (Tamargo et al., 2022), we possessed little insight into the impact of nanoplastic exposure on the gut microbiome especially at the short timeframes studied here. Prior work at longer exposure timeframes has revealed that nanoplastics elicit more severe effects on the gut microbiome than microplastics, at least in zebrafish (Xie et al., 2021), and that exposure to nanoplastics facilitates gut barrier dysfunction and intestinal translocation of microbiota in mice (Qiao et al., 2021). Our investigation finds that both exposure to 20 and 200 nm plastic exposure can significantly impact the composition of the gut microbiome even 25.5 h after exposure. This difference was surprising given that we may not expect such extreme alterations to quickly emerge as a result of differential preferences in microbial growth rates. However, plastic exposure may be especially toxic to some gut bacteria, possibly due to their activation of the immune system, which may result in rapid loss of specific microbial taxa. Such a finding suggests that plastic exposure may not trigger immune activation *via* microbiome perturbation, though it is important to note that immune activation cascades can result from immune activated dysbiosis (Vindigni et al., 2016). Consequently, future work should explore whether nanoplastic exposure drives chronic immune activation as a result of its disruption to the gut microbiome.

Lytic cell death was apparent only in small intestine of mice 25.5 h after 200 nm PSNS treatment. However, time after treatments was without effect on counts of cells expressing cleaved caspase-3 as determined by IHC (Table 1). Counts of cleaved caspase-3 immunolabeled cells were statistically different after PSNS treatments (Table 1). This suggested activation of caspase-3 preceded lytic cell death, and that 200 nm PSNS induced either more efficient or rapid cell death. It was not possible to distinguish between pyroptosis or necroptosis with TEM and expression of a limited number of genes. Regardless, lytic cell death in enterocytes perhaps disrupted barrier function of the gut and contributed to entry of 200 nm PSNS into the blood and decreased biodiversity of the microbiome. Newton et al. reviewed pathological responses, their molecular level underpinning, and factors that triggered them. Caspase-3 activation was consistent with pyroptosis (Newton et al., 2021). The small intestine of adult mice is about 30–40 cm. Adequately sampling a structure of this length with a potentially low frequency of dead cells with 5 μm sections can result in bias and results should be interpreted cautiously. However, evidence of lytic cell death by both IHC and TEM suggests relevance of these observations and the associated processes. Nanoscale (oxidized low-density lipoprotein and amyloid-beta protein) and microscale (monosodium urate and cholesterol crystals) sterile particles can lead to pyroptosis. Further, in a mouse model for autoimmune disease rare dying cells promoted inflammation, and lytic cell death in small numbers of enterocytes were potential early events in gut inflammation (Newton et al., 2021). Therefore, further evaluation of the potential role for nanoplastics in the context of inflammatory bowel disease is warranted.

Data availability statement

The raw sequence files generated during the current study are available at the NCBI Sequence Read Archive (SRA) project number PRJNA831840.

Ethics statement

The animal study was reviewed and approved by Institutional Animal Care and Use Committee (IACUC) at Oregon State University.

Author contributions

JS, LC, TS, CL, SB, and SLH contributed to the conception and design of the study. JS and LC wrote the manuscript. JS conducted transmission electron microscopy and analysis. LC oversaw gavage experiments and tissue collection. TS, MS, and KK conducted gut microbiota analysis. CL conducted immunohistochemistry and pathology analysis. SB, JP, and SJH conducted gene expression analysis. All

authors contributed to manuscript revision and approved the submitted version.

Acknowledgments

JS acknowledges support from the Image Analysis Laboratory in the College of Veterinary Medicine at Texas A&M University (RRID: SCR 022479) and the Histology section in the Oregon Veterinary Diagnostic Laboratory. The Oregon Agricultural Experiment Station funded LC for this project. TS was funded by the National Institute of Environmental Health Sciences (NIEHS) of the National Institutes of Health, award number 1R01 ES030226. SLH and SB were funded by the National Science Foundation Growing Convergence Research Big Idea, award number 1935028.

Conflict of interest

The authors declare that the research was conducted in the absence of any commercial or financial relationships that could be construed as a potential conflict of interest.

Publisher's note

Supplementary material

The Supplementary Material for this article can be found online at: https://www.frontiersin.org/articles/10.3389/frwa.2022.925781/full#supplementary-material

SUPPLEMENTARY FIGURE 1
Control PSNS stained with ruthenium tetroxide and imaged by transmission electron microscopy. **(A)** Densely stained control 20 nm PSNS were detected in isolation (see arrowheads for examples) or in clumps (see arrows for examples). The diameters of 228 isolated beads were measured to be 20.9 ± 6.7 nm. **(B)** Densely stained control 200 nm PSNS. The diameters of 242 isolated beads were measured to be 247.4 ± 57.7 nm. Scale = 0.5 μm.

SUPPLEMENTARY FIGURE 2
Gene expression results in the **(A)** liver and **(B)** small intestine for control, 20 nm, and 200 nm PSNS exposures. Mice were exposed for 25.5 h. Data is expressed as delta CT. No significant differences in gene expression after PSNS exposure were detected (*cyp1b1* in liver $p = 0.0767$, all other genes $p > 0.1$, one-way ANOVA).

SUPPLEMENTARY TABLE 1
Primer sequences used for gene expression analysis. Primers for IL22, GR, Catalase, SOD1, Claudin2, Occludin, TJP1, and GAPDH were purchased from Integrated DNA Technologies—IDT (Coralville, IA), and primers for Cyp1b1 were purchased from SA Biosciences as part of QIAGEN (Hilden, Germany).

SUPPLEMENTARY TABLE 2
Enterocytes immunolabeled for cleaved caspase-3 in duodenums from mice treated with vehicle or PSNS (20 or 200 nm) collected at two time points after exposure.

References

Adar, F., Mamedov, S., and Whitley, A. (2005). Limits of spatial resolution of a raman microscope. *Microsc. Microanal.* 11, 728–728. doi: 10.1017/S1431927605507384

Al-Sid-Cheikh, M., Rowland, S. J., Stevenson, K., Rouleau, C., Henry, T. B., and Thompson, R. C. (2018). Uptake, whole-body distribution, and depuration of nanoplastics by the scallop pecten maximus at environmentally realistic concentrations. *Environ. Sci. Technol.* 52, 14480–14486. doi: 10.1021/acs.est.8b05266

Borrelle, S. B., Ringma, J., Law, K. L., Monnahan, C. C., Lebreton, L., McGivern, A., et al. (2020). Predicted growth in plastic waste exceeds efforts to mitigate plastic pollution. *Science* 369, 1515–1518. doi: 10.1126/science.aba3656

Brahney, J., Mahowald, N., Prank, M., Cornwell, G., Klimont, Z., Matsui, H., et al. (2021). Constraining the atmospheric limb of the plastic cycle. *Proc. Natl. Acad. Sci. U.S.A.* 118, e2020719118. doi: 10.1073/pnas.2020719118

Brander, S. M., Renick, V. C., Foley, M. M., Steele, C., Woo, M., Lusher, A., et al. (2020). Sampling and quality assurance and quality control: a guide for scientists investigating the occurrence of microplastics across matrices. *Appl. Spectrosc.* 74, 1099–1125. doi: 10.1177/0003702820945713

Chatuphonprasert, W., and Jarukamjorn, K. (2021). Effect of styrene oxide and diethyl maleate on expression of cytochrome P450 family 1 and glutathione store in mouse liver. *Trop. J. Pharm. Res.* 20, 231–237. doi: 10.4314/tjpr.v20i2.2

Coffin, S., Bouwmeester, H., Brander, S. M., Damdimopoulou, P., Gouin, T., Hermabessiere, L., et al. (2022). Development and application of a health-based framework for informing regulatory action in relation to exposure of microplastic particles in California drinking water. *Microplast. Nanoplast.* 2, 12. doi: 10.1186/s43591-022-00030-6

Cowger, W., Gray, A., Christiansen, S. H., DeFrond, H., Deshpande, A. D., Hemabessiere, L., et al. (2020). Critical review of processing and classification techniques for images and spectra in microplastic research. *Appl. Spectrosc.* 74, 989–1010. doi: 10.1177/0003702820929064

Cox, K. D., Covernton, G. A., Davies, H. L., Dower, J. F., Juanes, F., and Dudas, S. E. (2019). Human consumption of microplastics. *Environ. Sci. Technol.* 53, 7068–7074. doi: 10.1021/acs.est.9b01517

DeCourten, B. M., Connon, R. E., and Brander, S. M. (2019). Direct and indirect parental exposure to endocrine disruptors and elevated temperature influences gene expression across generations in a euryhaline model fish. *PeerJ* 7, e6156. doi: 10.7717/peerj.6156

Deng, Y., Zhang, Y., Lemos, B., and Ren, H. (2017). Tissue accumulation of microplastics in mice and biomarker responses suggest widespread health risks of exposure. *Sci. Rep.* 7, 46687. doi: 10.1038/srep46687

Desai, N., AbdelHafez, F., Drazba, J., Goldfarb, J., and Falcone, T. (2010). A simple and efficient method for preparation of isolated ovarian follicles for transmission electron microscopy. *J. Assist. Reprod. Genet.* 27, 97–101. doi: 10.1007/s10815-010-9389-4

Garcia, G. R., Shankar, P., Dunham, C. L., Garcia, A., La Du, J. K., Truong, L., et al. (2018). Signaling events downstream of AHR activation that contribute to toxic responses: the functional role of an AHR-dependent long noncoding

RNA (slincR) using the zebrafish model. *Environ. Health Perspect.* 126, 117002. doi: 10.1289/EHP3281

Gouin, T. (2020). Toward an improved understanding of the ingestion and trophic transfer of microplastic particles: critical review and implications for future research. *Environ. Toxicol. Chem.* 39, 1119–1137. doi: 10.1002/etc.4718

Granby, K., Rainieri, S., Rasmussen, R. R., Kotterman, M. J. J., Sloth, J. J., Cederberg, T. L., et al. (2018). The influence of microplastics and halogenated contaminants in feed on toxicokinetics and gene expression in European seabass (*Dicentrarchus labrax*). *Environ. Res.* 164, 430–443. doi: 10.1016/j.envres.2018.02.035

Hodges, R. E., and Minich, D. M. (2015). Modulation of metabolic detoxification pathways using foods and food-derived components: a scientific review with clinical application. *J. Nutr. Metab.* 2015, 760689. doi: 10.1155/2015/760689

Kostic, A. D., Xavier, R. J., and Gevers, D. (2014). The microbiome in inflammatory bowel disease: current status and the future ahead. *Gastroenterology* 146, 1489–1499. doi: 10.1053/j.gastro.2014.02.009

Kundu, P., Torres, E. R. S., Stagaman, K., Kasschau, K., Okhovat, M., Holden, S., et al. (2021). Integrated analysis of behavioral, epigenetic, and gut microbiome analyses in App(NL-G-F), App(NL-F), and wild type mice. *Sci. Rep.* 11, 4678. doi: 10.1038/s41598-021-83851-4

Lasch, P., and Naumann, D. (2006). Spatial resolution in infrared microspectroscopic imaging of tissues. *Biochim. Biophys. Acta* 1758, 814–829. doi: 10.1016/j.bbamem.2006.06.008

Leslie, H. A., van Velzen, M. J. M., Brandsma, S. H., Vethaak, A. D., Garcia-Vallejo, J. J., and Lamoree, M. H. (2022). Discovery and quantification of plastic particle pollution in human blood. *Environ. Int.* 163, 107199. doi: 10.1016/j.envint.2022.107199

Li, B., Ding, Y., Cheng, X., Sheng, D., Xu, Z., Rong, Q., et al. (2020). Polyethylene microplastics affect the distribution of gut microbiota and inflammation development in mice. *Chemosphere* 244, 125492. doi: 10.1016/j.chemosphere.2019.125492

Livak, K. J., and Schmittgen, T. D. (2001). Analysis of relative gene expression data using real-time quantitative PCR and the 2(-Delta Delta C(T)) method. *Methods* 25, 402–408. doi: 10.1006/meth.2001.1262

Lu, K., Abo, R. P., Schlieper, K. A., Graffam, M. E., Levine, S., Wishnok, J. S., et al. (2014). Arsenic exposure perturbs the gut microbiome and its metabolic profile in mice: an integrated metagenomics and metabolomics analysis. *Environ. Health Perspect.* 122, 284–291. doi: 10.1289/ehp.1307429

McShane, B. B., Gal, D., Gelman, A., Robert, C., and Tackett, J. L. (2019). Abandon statistical significance. *Am. Stat.* 73, 235–245. doi: 10.1080/00031305.2018.1527253

Mohamed Nor, N. H., Kooi, M., Diepens, N. J., and Koelmans, A. A. (2021). Lifetime Accumulation of microplastic in children and adults. *Environ. Sci. Technol.* 55, 5084–5096. doi: 10.1021/acs.est.0c07384

Naslavsky, N., and Caplan, S. (2018). The enigmatic endosome - sorting the ins and outs of endocytic trafficking. *J. Cell Sci.* 131, jcs216499. doi: 10.1242/jcs.216499

Newton, K., Dixit, V. M., and Kayagaki, N. (2021). Dying cells fan the flames of inflammation. *Science* 374, 1076–1080. doi: 10.1126/science.abi5934

Pandey, E., Nour, A. S., and Harris, E. N. (2020). Prominent receptors of liver sinusoidal endothelial cells in liver homeostasis and disease. *Front. Physiol.* 11, 873. doi: 10.3389/fphys.2020.00873

Qiao, J., Chen, R., Wang, M., Bai, R., Cui, X., Liu, Y., et al. (2021). Perturbation of gut microbiota plays an important role in micro/nanoplastics-induced gut barrier dysfunction. *Nanoscale* 13, 8806–8816. doi: 10.1039/D1NR00038A

Revel, M., Chatel, A., and Mouneyrac, C. (2018). Micro(nano)plastics: a threat to human health? *Curr. Opin. Environ. Sci. Health* 1, 17–23. doi: 10.1016/j.coesh.2017.10.003

Rivlin, P. K., and Raymond, P. A. (1987). Use of osmium tetroxide-potassium ferricyanide in reconstructing cells from serial ultrathin sections. *J. Neurosci. Methods* 20, 23–33. doi: 10.1016/0165-0270(87)90036-7

Round, J. L., and Mazmanian, S. K. (2009). The gut microbiota shapes intestinal immune responses during health and disease. *Nat. Rev. Immunol.* 9, 313–323. doi: 10.1038/nri2515

Schneider, C. A., Rasband, W. S., and Eliceiri, K. W. (2012). NIH image to ImageJ: 25 years of image analysis. *Nat. Methods* 9, 671–675. doi: 10.1038/nmeth.2089

Schulze, R. J., Schott, M. B., Casey, C. A., Tuma, P. L., and McNiven, M. A. (2019). The cell biology of the hepatocyte: a membrane trafficking machine. *J. Cell Biol.* 218, 2096–2112. doi: 10.1083/jcb.201903090

Senathirajah, K., Attwood, S., Bhagwat, G., Carbery, M., Wilson, S., and Palanisami, T. (2021). Estimation of the mass of microplastics ingested - a pivotal first step towards human health risk assessment. *J. Hazard. Mater.* 404 (Pt. B), 124004. doi: 10.1016/j.jhazmat.2020.124004

Senathirajah, K., and Palanisami, T. (2019). *No Plastic in Nature: Assessing Plastic Ingestion From Nature to People.* Gland: World Wide Fund for Nature.

Sommi, P., Vitali, A., Coniglio, S., Callegari, D., Barbieri, S., Casu, A., et al. (2021). Microvilli adhesion: an alternative route for nanoparticle cell internalization. *ACS Nano* 15, 15803–15814. doi: 10.1021/acsnano.1c03151

Stubbins, A., Law, K. L., Munoz, S. E., Bianchi, T. S., and Zhu, L. (2021). Plastics in the earth system. *Science* 373, 51–55. doi: 10.1126/science.abb0354

Tamargo, A., Molinero, N., Reinosa, J. J., Alcolea-Rodriguez, V., Portela, R., Banares, M. A., et al. (2022). PET microplastics affect human gut microbiota communities during simulated gastrointestinal digestion, first evidence of plausible polymer biodegradation during human digestion. *Sci. Rep.* 12, 528. doi: 10.1038/s41598-021-04489-w

Trent, J. S., Scheinbeim, J. I., and Couchman, P. R. (1983). ruthenium tetraoxide staining of polymers for electron microscopy. *Macromolecules* 16, 589–598. doi: 10.1021/ma00238a021

Tu, P., Chi, L., Bodnar, W., Zhang, Z., Gao, B., Bian, X., et al. (2020). Gut microbiome toxicity: connecting the environment and gut microbiome-associated diseases. *Toxics* 8, 19. doi: 10.3390/toxics8010019

Vindigni, S. M., Zisman, T. L., Suskind, D. L., and Damman, C. J. (2016). The intestinal microbiome, barrier function, and immune system in inflammatory bowel disease: a tripartite pathophysiological circuit with implications for new therapeutic directions. *Therap. Adv. Gastroenterol.* 9, 606–625. doi: 10.1177/1756283X16644242

Walters, W., Hyde, E. R., Berg-Lyons, D., Ackermann, G., Humphrey, G., Parada, A., et al. (2016). Improved bacterial 16S rRNA Gene (V4 and V4-5) and fungal internal transcribed spacer marker gene primers for microbial community surveys. *mSystems* 1, e00009–15. doi: 10.1128/mSystems.00009-15

Wan, Z., Wang, C., Zhou, J., Shen, M., Wang, X., Fu, Z., et al. (2019). Effects of polystyrene microplastics on the composition of the microbiome and metabolism in larval zebrafish. *Chemosphere* 217, 646–658. doi: 10.1016/j.chemosphere.2018.11.070

Wright, S. L., and Kelly, F. J. (2017). Plastic and human health: a micro issue? *Environ. Sci. Technol.* 51, 6634–6647. doi: 10.1021/acs.est.7b00423

Xie, S., Zhou, A., Wei, T., Li, S., Yang, B., Xu, G., et al. (2021). Nanoplastics induce more serious microbiota dysbiosis and inflammation in the gut of adult zebrafish than microplastics. *Bull. Environ. Contam. Toxicol.* 107, 640–650. doi: 10.1007/s00128-021-03348-8

Yong, C. Q. Y., Valiyaveetill, S., and Tang, B. L. (2020). Toxicity of microplastics and nanoplastics in mammalian systems. *Int. J. Environ. Res. Public Health* 17, 1509. doi: 10.3390/ijerph17051509

Zhang, J. Q., Zhou, W., Zhu, S. S., Lin, J., Wei, P. F., Li, F. F., et al. (2017). Persistency of enlarged autolysosomes underscores nanoparticle-induced autophagy in hepatocytes. *Small* 13, e20160876. doi: 10.1002/smll.201602876